Frustrated electrons on a spatially anisotropic triangular lattice: Emergent competition of charge orders and exotic disorders due to thermal fluctuations

Tempei Yoshida
Department of Physics, Kyoto Sangyo University, Kyoto 603-8555, Japan

Chisa Hotta
Department of Basic Science, The University of Tokyo, 3-8-1 Komaba, Meguro, Tokyo 153-8902, Japan

(Received 28 September 2014; revised manuscript received 20 November 2014; published 5 December 2014)

We study the interplay of correlation and thermal fluctuation in a system consisting of two species of classical particles with up and down spin on a geometrically frustrated anisotropic triangular lattice, described by an extended four-state Potts model. The model corresponds to the strong coupling limit of the extended Hubbard model at quarter-filling, which is known to host several competing charge ordered phases as well as an exotic quantum state called pinball liquid. The frustrated intersite Coulomb interactions together with the on-site Coulomb interaction generate macroscopically degenerate manifolds of low-energy states. They compete entropically at finite temperature and two characteristic states emerge; a threefold periodic charge ordered state and a quasi-one-dimensionally disordered state called "good defect state" characterized by the systematic generation of ferroelectric bonds. The two states show good correspondence with the threefold charge order and the pinball liquid in the extended Hubbard model, and are separated by the partial Mott transition taking place on one of the three sublattices of the triangular lattice.

DOI: 10.1103/PhysRevB.90.245115 PACS number(s): 71.10.−w, 71.23.−k, 71.30.+h, 75.40.−s

I. INTRODUCTION

The geometrical frustration effect in magnets has been a topic of constant interest due to a variety of phenomena it provides [1], such as spin liquids [2], nematic orders [3], glasses without extrinsic disorders [4–6], spin chirality [7], and spin ices [8]. Frustration arises when there is no way of arranging spins that could satisfy all the interactions simultaneously, e.g., when spins are aligned on triangular, kagome, or pyrochlore lattices, etc. Even for such single spin degrees of freedom, a frustration effect is already a challenging many-body problem. In solids, however, there are more numbers of degrees of freedom, namely, spins, charges, orbitals, and lattices that often come into play in their low-energy properties, giving rise to far richer phenomena. In such presence of many degrees of freedom, the frustration effect is quite elusive.

Among them, one could find a relatively simple and almost solvable example in a class of quarter-filled strongly correlated electronic systems, where the interplay of geometrical frustration with the electronic correlation could be observed [9]; consider strong intersite interactions between electrons along the nearest neighbor sites of a triangular lattice denoted as V and V' (see the inset of Fig. 2), together with the on-site Coulomb interaction U. At quarter-filling, there is one electron per two sites on average, and if the frustration is weak and the interactions are strong enough, $U \gg V > V'$, the electrons form a regular staggered ordered pattern [see Fig. 2(a)] on the square lattice formed by V bonds to avoid both the double occupancy (U) and the neighboring occupancy along the V bonds. In approaching a regular triangular lattice, $V' \sim V$, the frustration increases and destroys this order, and some unexpected phases may emerge, which is the topic of the present paper.

In geometrically frustrated systems, the competition between different exchange interactions generates a massive classical ground state degeneracy. These states are extremely sensitive to degeneracy breaking perturbations. An example is the intersite hopping integrals, t, of the electrons in solids in the strong coupling (classical) limit, $t/U, t/V \to 0$. This quantum fluctuation mixes the degenerate ground state manifold and helps to form an ordered state out of classical disorder. The degeneracy in the free energy is also lifted entropically, namely, by the thermal fluctuation, and the so-called "order-by-disorder" may take place with increasing temperatures [10]. While both of these effects play an important role to understand the behavior of frustrated electrons, the two effects are easily mixed up, which complicates a plot. In the present paper, we focus only on the effect of thermal fluctuation, and neglect the quantum fluctuation, setting $t = 0$. Then, the issue is simplified to the classical energetics: four different states with different energies are allowed per one lattice site, namely (0),(↑), (↓), and (↑↓), with ↑ and ↓ representing the electrons of that spin orientation, which are characterized by the number of charges, $n_i = 0,1,1,2$, respectively, with the total number of

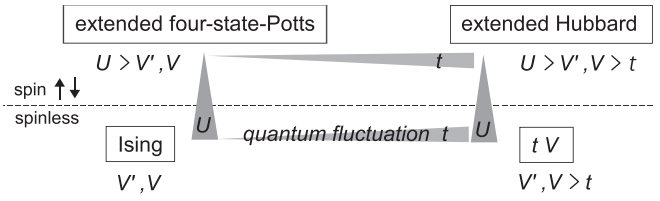

FIG. 1. Schematic relationships between four models: extended four-state Potts model with U and V, V'; extended Hubbard model with U, V, V', and t; Ising model with V and V' without spin degrees of freedom; spinless fermionic t-V model with V, V', and t. The pinball liquid phase [21] appears in both the extended Hubbard and t-V models, and its classical limit corresponds to the defect state in the other two models.

particles fixed to quarter-filling. Since the interactions between neighboring pair of sites are the multiple of how many charges each hold, the model could be regarded as an extension of the classical four-state Potts model [11].

Our extended four-state Potts model has relevance to two interesting cases (see Fig. 1). First, if we take $U = \infty$ limit, the spin degrees of freedom just gives the trivial macroscopic degeneracy of $2^{N_\uparrow + N_\downarrow}$, and its intrinsic property is reproduced to the Ising model, the basic model in statistical physics. Although its exact solution is already found in 1950 [12,13], its microscopic features at low temperatures are clarified in detail only recently [14]. There, it is found that the low-energy states are governed by the systematic domain-wall excitations (which is called defects, see Sec. II for details), while the system remains disordered throughout the whole temperature region. The introduction of additional longer-range attractive interactions is found to drive the system to the Berezinskii-Kosterlitz-Thouless transition at a finite temperature [15].

The other relevant case of the extended four-state Potts model is realized by the introduction of the intersite transfer integral, t and t' (following the same notation of anisotropy with V and V'), where we have a realistic strongly correlated electron system represented by the extended Hubbard model at 3/4-filling. Its ground state phase diagram is explored by several different numerical approaches [16–18]. At relatively small $U/t \lesssim 15$, there are three different kinds of charge ordered (CO) phases. The two are the different geometry of stripes, both with a twofold periodicity of charges along V and V' bonds, respectively [basically the same as those given in Figs. 2(a) and 2(b)]. The other is the threefold periodic charge order; in dividing the system into three sublattices, all the sites in one sublattice is occupied by more than one electron, and the other two-third of the sites have very small amount of charges, which form a bad metal. At larger U region, the constraint of nearly no double occupancy on each site converts this bad metal to a more exotic metallic state called "pinball liquid" [19,20], which one of the authors has previously proposed in the spinless fermionic model in Ref. [21], and is studied in more detail in other filling recently [22]. The pinball liquid in the extended Hubbard model is found to show a heavy fermionic behavior [23], and shows a quantum criticality at low temperature near the CO phase transition [19,20].

The extended Hubbard model is considered to give a minimal theoretical description of the electronic properties of θ-ET_2X organic solids, wherein many intriguing phenomena that could possibly be attributed to the electronic frustration are experimentally observed [9], e.g., a sign of inhomogeneity [24], nonlinear conductivity [25], and a formation of charge cluster glass [26] in the metallic state in the vicinity of charge ordered insulating phase. θ-ET_2X has a layered crystal structure, and the electronic states on the conducting layer is formed based on the anisotropic triangular lattice structure of the highest occupied molecular orbitals(HOMO) of ET molecules 3/4-filled on an average. The intersite Coulomb interactions, V and V', between these HOMO's are possibly frustrated, and stripe CO phase as well as quasi-three-fold periodic short-range order, with not exactly the same spatial structures (wave numbers) [27] but similar to the ones found in the extended Hubbard model [33], are experimentally

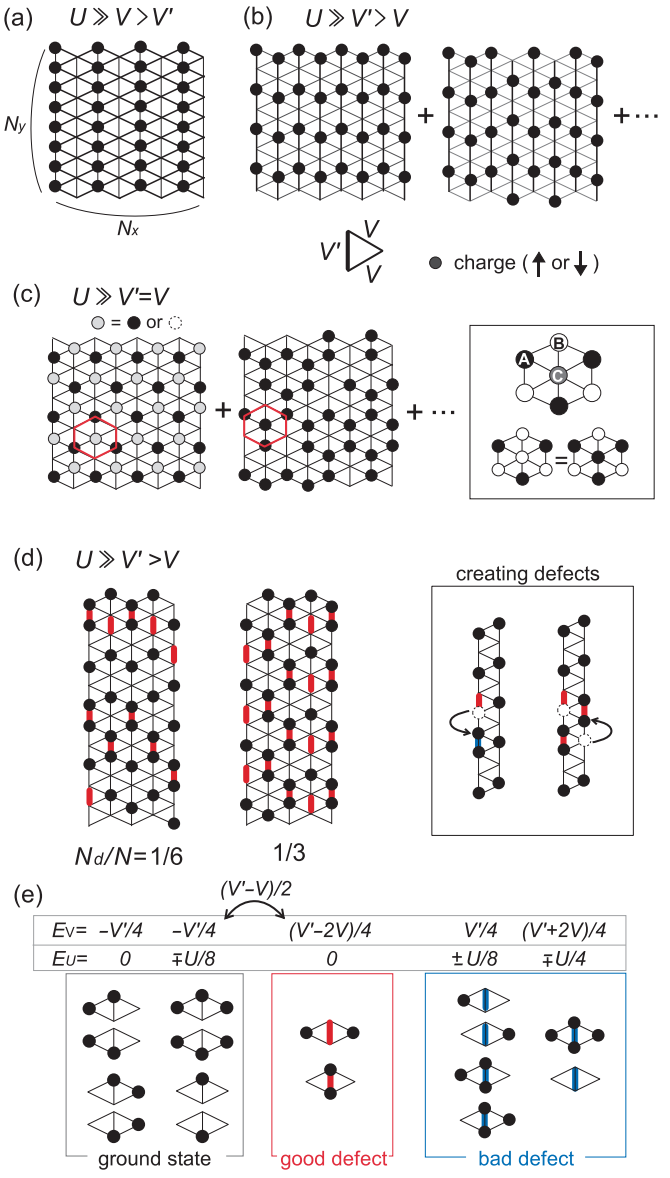

FIG. 2. (Color online) Ground states (a)–(c) and the low-energy state (d) of Eq. (1) at $U \gg V, V'$ which do not have double occupancy on all lattice sites. Bullet represents a single occupation of particle with either up or down spin. Panels show (a) vertical stripe charge order at $V > V'$ [$E = (V' - 2V)N/4$], (b) chain stripe order at $V' > V$ ($E = -V'N/4$) at which the interchain direction (x-direction) is disordered, (c) three sublattice disordered state [$E = -(V' + 2V)N/12$] with macroscopic degeneracy. See the texts for details. In (d), two different configurations of "good defect state", the low-energy excited states at $V' > V$, are shown. They host only the defects with lowest energy excitations, marked with red bonds. Examples of creating defects is shown in the right panel. (e) Energy of plaquettes with and without defects, where E_V and E_U represent the energy of the first and second term in Eq. (1), respectively. The ground state consists of eight different plaquettes without defects. The good defects have the lowest excitation energy, $\Delta E = (V' - V)/2$. The contribution from the U term is canceled out on the whole as the total number of particle is fixed and there is no double occupancy. In order to exclude bad defects with higher energies, the good defects need to align alternatively between all the neighboring chains. The number of good defect per chain is fixed, with its total number, N_d.

observed. We discuss briefly the relevance of our results with these experiments in the final section.

The present paper discloses the whole finite temperature phases of the extended four-state Potts model, which then helps to understand the nature of the above mentioned relevant models from two aspects; one is to clarify the role of the thermal fluctuation effect of the extended Hubbard model by disregarding the quantum fluctuations. The other is to understand the role of spin degrees of freedom at finite temperature through the comparison with the "spinless" Ising model. We also show that the pinball liquid phase in the t-V and extended Hubbard models is understood as an analog of the the exotic low-temperature phase in the Ising model characterized by the defect excitation [14], and that the transition from the threefold charge order to the pinball liquid phases could be regarded as a partial Mott transition.

The paper is organized as follows. In Sec. II, we introduce the model and its possible low-energy states, which actually appear in our numerical results. We present our results in Sec. III based on the classical Monte Carlo approach within the framework of Wang-Landau method, and discuss the relevance with other models as well as experiments in Sec. IV. A short summary and outlooks are given in Sec. V.

II. MODEL AND LOW-ENERGY STRUCTURES

A. Model Hamiltonian

Throughout this paper, we consider the extended four-state Potts model on an anisotropic triangular lattice, which has two species of particles characterized by up and down spins. The Hamiltonian is given as

$$\mathcal{H} = \sum_{\langle ij \rangle} V_{ij} \left(n_i - \frac{1}{2} \right) \left(n_j - \frac{1}{2} \right) + \sum_{i=1}^{N} U \left(n_{i\uparrow} - \frac{1}{2} \right) \left(n_{i\downarrow} - \frac{1}{2} \right), \quad (1)$$

where $n_{j\sigma}$ denotes the particle on jth site with index $\sigma(=\uparrow,\downarrow)$ and $n_j = n_{j\uparrow} + n_{j\downarrow}$. The on-site and intersite interactions, U and $V_{ij} = V$ and V', are given in Fig. 2(a), where we consider a rectangular cluster of size $N = N_x \times N_y$, and refer to the y direction as chain direction. The summation in the first term runs over all pairs of neighboring sites $\langle ij \rangle$. As we discussed earlier, each lattice site holds four different states, (0), (↑), (↓), and (↑↓), and each species of particle is not allowed to have double occupancy. The total particle number is fixed to quarter-filling, $N_\uparrow + N_\downarrow = N/2$, and only the nonmagnetic states are considered, which does not deteriorate the results. Note that due to the particle-hole symmetry, the case of 3/4-filling gives the identical results.

Let us first briefly mention the relationships with the other models. The extended Hubbard model Hamiltonian is given by adding the transfer integral, t_{ij}, to Eq. (1) as

$$\mathcal{H}_{\rm ETH} = \sum_{\langle i,j \rangle,\sigma} t_{ij} (c^\dagger_{i\sigma} c_{j\sigma} + \text{H.c.}) + \sum_{\langle i,j \rangle} V_{ij} n_i n_j + \sum_i U n_{i\uparrow} n_{i\downarrow}, \quad (2)$$

where $c^\dagger_{j\sigma}$ ($c_{j\sigma}$) is the creation (annihilation) operator of electron with spin $\sigma(=\uparrow,\downarrow)$ on j-th site, with $n_{j\sigma} = c^\dagger_{j\sigma} c_{j\sigma}$. The second and third term is identical to Eq. (1) besides the constant term, $-N(V' + 2V)/4$, which formally gives the particle-hole symmetry.

On the other hand, by taking the $U/V_{ij} = \infty$ limit of Eq. (1) and disregarding the spin degrees of freedom, the Ising model is obtained as

$$\mathcal{H}_{\rm ising} = \sum_{\langle i,j \rangle} V_{ij} \left(n_i - \frac{1}{2} \right) \left(n_j - \frac{1}{2} \right). \quad (3)$$

The absence and presence ($n_i = 0$ and 1) of the particle at each site represent the two Ising levels.

B. Characterization of low-energy states

In the four-state Potts model, there are several regular alignments of particles as shown schematically in Figs. 2 and 3. When the double occupancy is absent at sufficiently large U, the low-energy states are basically identical with those of the Ising model besides the trivial $2^{N_\uparrow + N_\downarrow}$fold spin degeneracy. Let us summarize these non-doubly-occupied configurations following Ref. [14]. In the ground state, there are two different stripe phases as the particles avoid the neighboring occupation along the strongest interaction bonds; at $V > V'$ the regular stripe along the chain direction with a unique configuration of particles [Fig. 2(a)], and for $V < V'$, the stripe with 2^{N_x}-fold degenerate configuration due to residual diagonal frustration, which we call "chain stripe" [Fig. 2(b)]. At $V = V'$ the two stripes become degenerate, and in addition, there is a

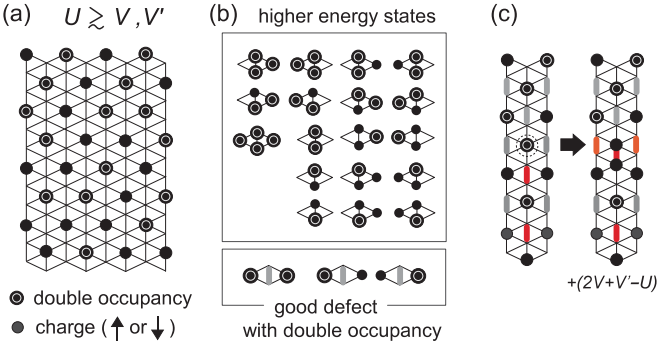

FIG. 3. (Color online) Ground state and low-energy states of Eq. (1) at $U \gtrsim V', V$, which include sites with double occupancy. (a) Ground state at relatively small U, consisting of $2N/3$ empty sites and $N/6$ singly occupied and $N/6$-doubly occupied sites, where $E = NU/6 - N(V' + 2V)/4$. The choices of singly and doubly occupied sites among one of the three sublattices are arbitrary. (b) Possible configurations of particles on a plaquette including doubly occupied sites. Another series of "good defects" with double occupancy on the left or right sides of the plaquette are described by gray bonds and are discriminated from others since their energy is comparable to those of the good defects in Fig. 2(e). (c) Left panel shows the ground state at $U \leqslant 3V$. By moving one particle from a doubly occupied site marked with broken circle to its neighbor in the right panel, the state with energy difference of $2V + V' - U$ is formed. The threefold CO state is converted to the good defect state in Fig. 2(d) by repeating this operation $N/6$ times.

macroscopically degenerate manifold of states called "uud" or "three-sublattice and its contingents" [21]. Dividing the system into three sublattices, and keeping one sublattice filled and another sublattice empty [Fig. 2(c)], and putting the rest of the particles ($N/6$) to the third sublattice randomly, we get the typical pattern known as "uud" in the Ising antiferromagnet (i.e., two up spins and one down spin per each triangle). There are numbers of neighboring particle-hole pairs that are allowed to exchange without changing the energy [see the inset of Fig. 2(c)], and numerous contingent degenerate states are generated. The pinball liquid state [21] is formed by the mixing of this three-sublattice and contingents by the introduction of t, and appear in the extended Hubbard model at large U as well as in the t-V model.

At $V' > V$, the ground state is the chain stripe charge order and its the low energy excitations are described by the particular class of domain walls called "good defects;" the simplest elementary particle excitation without double occupancy is to create a vertical (V') bond whose both edge sites are occupied either by particles or by holes, which we call "defects" [see Fig. 2(d)]. The energy of defects are classified according to the occupation number of their two adjacent sites on the neighboring chains [see the figure in unit of plaquette in the right panel of Fig. 2(e)], and two of the defect plaquettes with the lowest energy are called "good defects." Each plaquette with good defect carries the energy of $(V' - V)/2$ in Eq. (3) compared to the plaquette without defect. When $V' - V$ is small enough, the good defect is expected to dominate the low-energy excitation. However, it is usually difficult to create only good ones. A random introduction of defects always creates both good and bad defects, e.g., when moving one particle along the V' bond by one lattice spacing as shown in the inset of Fig. 2(d), a pair of both good and bad defects are created. Then, by creating another defect in the neighboring chain in between these good and bad defects, the bad defect is converted to the good ones. In this way, as the plaquettes share their edges with other plaquettes, they are always correlated with the ones on the neighboring chains. Thus one needs to follow a rule to exclude bad defects (see Ref. [14]); in each neighboring set of chains, the good defects should be inserted alternatively between left and right chains. This gives a strict constraint on the number of defects; all the chains must hold the same number of good defects, N_d/N_x. Once this rule is fulfilled, the excitation energy of the good defect states are given as, $N_d \times (V' - V)/2$, which is an extensive variable. A manifold of good defect state with the fixed number of N_d has massive degeneracy larger than that of the ground state. Considering the fact that each defect occupies N/N_d sites on an average, estimation of the degeneracy amounts to $(N/N_d)^{N_d}$ by the maximum term method, which is the lower bound. As it is larger than that of the chain stripe, the good defect state appears at low temperature in the Ising model at $V' > V \geqslant V'/2$, taking over the chain stripe ground state.

Note that the three-sublattice and contingent states given in Fig. 2(c) is identical to the good defect state with $N_d/N = 1/3$ [Fig. 2(d)], which we actually confirmed numerically in the finite cluster. In fact, the energy of the good defect state is given as $-V'N/4 + N_d(V' - V)/2$, which is $-(V' + 2V)N/12$ at $N_d/N = 1/3$.

TABLE I. Energy per site, E/N, and the degree of degeneracy, W, of three different classical manifolds of states, chain stripe [Fig. 2(b)], threefold CO [Fig. 3(a)], and good defect states without double occupancy [Fig. 2(d)]. $n_d = N_d/N$ denotes the defect density. Since the exact value of W of the good defect state is analytically not available, we give its lower bound, evaluated by the maximum term method. Our calculation shows that it is larger than the chain stripe by powers, $m = 1 - 2$ (see the density of states in Appendix B and Fig. 14).

	chain stripe	threefold CO	good defect
E/N	$-V'/4$	$U/6-(V'+2V)/4$	$-V'/4+n_d(V'-V)/2$
W	$2^{N_x} \times 2^{N/2}$	${}_{N/3}C_{N/6} \times 2^{N/6}$	$\sim (N/N_d)^{N_d} \times 2^{N/2}$

If we allow the double occupancy of sites by reducing U/V_{ij}, another series of low-energy states emerge. Figure 3(a) shows the threefold CO phase; among three of the sublattices, two are empty and one is occupied by 3/2 particles on an average. The choice of the doubly occupied sites among the $N/3$ sites together with the choice of spin alignments of the singly occupied sites, give the ${}_{N/3}C_{N/6} \times 2^{N/6}$-fold degeneracy.

One could see that this threefold CO has similar structure with the good defect state at $N_d/N = 1/3$. In fact, if we include another series of defects with double occupancy shown in the lower panel of Fig. 3(b) as members of good defects, the threefold CO state is described as $N_d/N = 1/3$ state, as shown in the left panel of Fig. 3(c). Here, by moving one particle from one doubly occupied site to its neighboring site along the V' bond, the good defect (without double occupancy) shifts by one lattice spacing, and the two gray bonds in the neighboring chains are transformed to the red ones without double occupancy. Such charge fluctuation costs the energy of $2V + V' - U$, which could be small enough when U is close to $2V + V'$.

Many of the representative states we discussed above have massive degeneracy, both due to the variation of the configuration of particles, and to the residual spin degrees of freedom, which we summarize in Table I. Since the higher excited states often have larger degeneracy, they could overtake the ground state at finite temperature depending on their relative energy differences, which is the main mechanism of the emergence of phases we discuss in the next section.

III. NUMERICAL ANALYSIS

A. Methods

We apply both the standard classical Markov chain Monte Carlo Method (MCMC) based on the Metropolis algorithm and the Wang-Landau method (WL) [34] to analyze Eq. (1). For MCMC, we take the thermal average of total 10^5 samplings from 20 independent runs, and obtain the main results from the typical system size of $(N_x, N_y) = (12,60)$.

At temperatures as low as $k_B T/V' \lesssim 0.1$, the statistical error of MCMC cannot be neglected, in which case the statistical average calculated from the density of states (see Appendix B) obtained by WL give a more reliable results. This should be because, the WL method gives accurate values

of density of states when its amplitude is large, and the present system in fact has large weights of states at low energy, typical of the frustrated system. For WL, we varied the modification factor from $f = \exp(1)$ up to $f \simeq \exp(10^{-3})$ by updating $f \to \sqrt{f}$ through about ten independent sweeps of random walk, and for each sweep we continue until the histogram converges to a flatness of less than 20% from the average. Due to the rapidly increasing number of sweeps and steps with increasing N, the maximum system size used in WL is limited. Therefore we confine ourselves to the relatively smaller size of the cluster, while carefully analyze the system size dependence of the results by comparing them with the MCMC and exact solutions (see Appendix A). In the following, we adopt the results at $N_x \times N_y = 8\times24$ and 8×48, based on WL thus obtained. Here, $N_x = 8$ is the minimum value of N_x, where the physical quantities no longer show size effect (see Appendix A). The reason why we take N_y much larger than N_x is that, in order to describe the good defects with low density, which appear near the zero temperature region, we need to take N_y as large as possible. The lowest good defect density available is $(N_d/N)_{\min} = 2/N_y$, since the smallest number of defect per chain is two under the periodic boundary condition. The results at $U = \infty$ successfully reproduced the results of the Ising model in Ref. [14] with $(N_x, N_y) = (50, 100)$ as we see shortly in Fig. 7 (see also Appendix A). Only when $N_d/N \lesssim (N_d/N)_{\min}$, N_g/N_d (but not other quantities like energy) shows a significant size effect as both N_d and N_g smaller than $2N_x$ (not enough to describe both the good defects and 1D disorder in Fig. 11) are not quantitatively reliable.

The finite temperature phase transition is detected by the divergence of the specific heat. In fact, we find two different types of ordered phases at low temperature, the stripe CO phase and the threefold CO, which are shown in Figs. 2(b) and 3(a), respectively. To accurately determine the phase transition point, we analyze the Binder parameter within the above mentioned sets of WL clusters, which is defined as

$$\mathcal{O}_B = 1 - \frac{\langle \mathcal{O}^4 \rangle}{3\langle \mathcal{O}^2 \rangle^2}. \tag{4}$$

For the threefold CO phase, we set the order parameter as

$$\mathcal{O}_i^{\text{3fold}} = \frac{\hexagon(i) - \langle \hexagon \rangle_d}{\langle \hexagon \rangle_3 - \langle \hexagon \rangle_d},$$

$$\hexagon(i) = \frac{1}{6}\sum_{\langle j,l \rangle}^{6} [2\text{sgn}(n_j) - 1][2\text{sgn}(n_l) - 1], \tag{5}$$

where the sum of neighboring sites, $\langle j,l \rangle$, is taken along the hexagonal bonds surrounding site i, and $\text{sgn}(n_j) = 1/0$ when the jth site is occupied (either singly or doubly)/unoccupied. In other words, $\hexagon(i)$ is the number density of ferrobonds subtracted by the number density of antiferrobonds on ith hexagon, and takes the value, $\langle \hexagon \rangle_3 = -1/3$ and $\langle \hexagon \rangle_d = 1/64$, in the threefold CO and fully disordered states, respectively.

B. Phase diagram

The phase diagram in the k_BT-V-U space in unit of $V' = 1$ is given in Fig. 4. At $T = 0$, the diagram is determined by comparing the energies of the characteristic states we discussed in Sec. II (see Table I). At $U/V \leqslant 3$, we find the threefold CO ground state [Fig. 3(a)], which is stabilized by making 1/6 of the sites doubly occupied in order to avoid the energy loss of neighboring occupancy along the V bonds. This threefold state is replaced by the chain stripe at large U

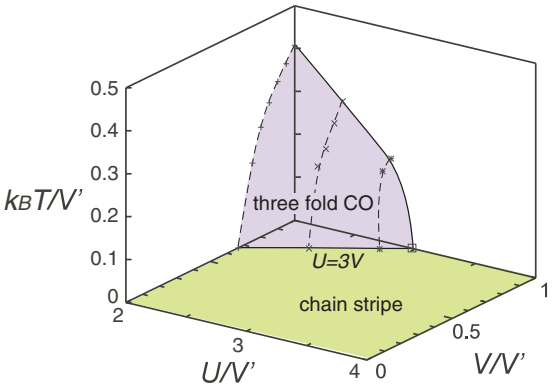

FIG. 4. (Color online) Phase diagram including the ground state and finite temperature as functions of V/V' and U/V'.

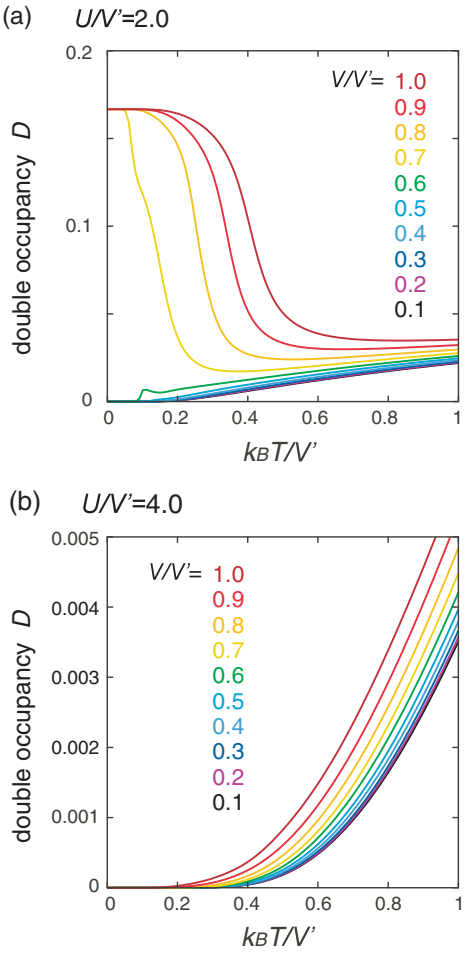

FIG. 5. (Color online) Temperature dependence of the double occupancy per site D at (a) $U/V' = 2$ and (b) $U/V' = 4$ for $V/V' = 0.1 - 1$, on a $N = 8\times24$ cluster by the WL method.

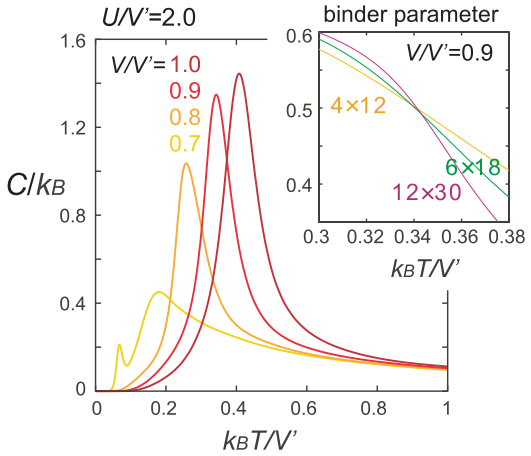

FIG. 6. (Color online) Specific heat C in unit of Boltzmann constant k_B calculated for $U/V' = 2$ at $V/V' = 0.7 - 1.0$ for $N = 8\times24$ cluster by the WL method. The peak indicates the transition between the disordered state and the threefold CO state. There is another lower peak found at $V/V' \lesssim 0.7$, while we confirmed that this point could not be described by the phase transition to any of the stripe phase. The inset shows the Binder parameter defined in Eq. (4) for the threefold CO order parameter Eq. (5) at $U/V' = 2$ and $V/V' = 0.9$, calculated for $N = 4\times12$, 6×18, and 12×30 clusters by the WL method. The crossing point magnified in the inset is well detected.

region, and the phase boundary between them are given as $U = 3V$. So far, we have considered only limited number of states, and the disordered states were not taken into account. To check whether the states other than Figs. 2 and 3 appear in the ground state, we numerically calculated the energy of the states over the whole Hilbert space in the small cluster. The obtained ground state phase diagram coincided with the one in Fig. 4.

At finite temperature, the state with the lowest free energy, $F = E - TS$, namely, those with relatively low energy and high entropy emerges. At $U/V \lesssim 3$, the threefold CO phase which appeared in the ground state is shown to survive up to the temperature of $k_BT \sim 0.4V'$. Figure 5(a) shows the double occupancy, $D = \langle n_{i\uparrow}n_{i\downarrow}\rangle$, calculated at $U = 2V'$. At $V/V' \geqslant 0.7$, the value of D rapidly increases at low temperature up to $D = 1/6$, which indicates that the threefold CO state with one-sixth of the sites being doubly occupied is realized. At smaller V and at larger U [see Fig. 5(b)], D continues to decrease down to zero with decreasing temperature, and the threefold CO phase no longer takes place.

The boundary between disordered phase and threefold CO is detected by the anomaly in the temperature dependence of the specific heat C. Figure 6 shows some examples at $U = 2V'$ for several choices of V/V'. While the specific heat shows a sharp peak indicating the divergence in its bulk limit, both its location and the power has cluster size dependence. To accurately determine the phase boundary, we further calculate the Binder parameter as shown in the inset of Fig. 6, and adopt the crossing point of several different clusters as phase transition point in the bulk limit.

C. Defect states

As we discussed in Sec. II B, the $U = \infty$ limit of the extended four state Potts model exactly correspond to the Ising model besides the trivial spin degeneracy. The low temperature region of the Ising model is dominated by the characteristic disordered state called "good defect state." This state consists of a manifold of degenerate configurations with only good defects generated alternatively between neighboring chains from the chain stripe ground state. The energy of this manifold is an extensive variable of the number of good defects N_g. Therefore it is numerically characterized by counting the number of good and bad defects in the MC steps. We first show in Figs. 7(a) and 7(b) the temperature dependence of the number density of good defects, N_g/N, and the ratio of good defects to the total number of defects, N_g/N_d, at this $U = \infty$ limit, which reproduces the results in Ref. [14]. With decreasing temperature and in approaching $V \sim V'$, the number of bad defects, $N_d - N_g$, decreases exponentially, and N_g/N_d approaches unity. At $V \sim V'$ and at low temperature, most of the defects are converted to good ones, and N_g/N

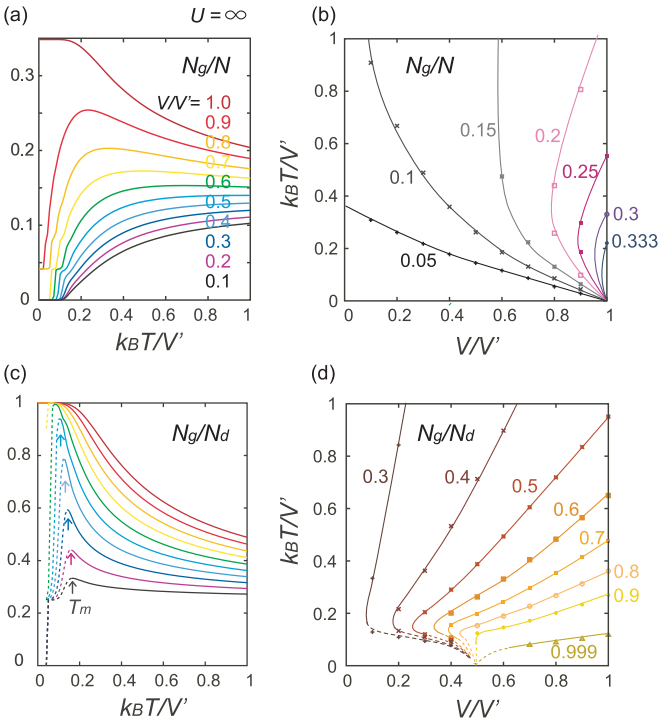

FIG. 7. (Color online) Analysis on the $U = \infty$ limit of the extended four state Potts model on a $N = 8\times48$ cluster, which corresponds to the Ising model in Eq. (3). (a) Temperature dependence and (b) contour plot of number density of good defect, N_g/N. (c) and (d) are those of the ratio of good defect to the total number of defects, N_g/N_d. The arrows in (c) indicate the crossover temperature T_m from a 2D disordered state at high temperature to 1D disordered states at low temperature (see Fig. 11). The value of N_g/N_d shows a size effect when $N_d/N \leqslant 2/48$, since the defect density there is lower than the one available for the present size of the cluster. The data in (c) and contour line (guide to the eye) in (d) in this region are shown in broken lines. The contour lines of (d) bundle into $V/V' = 0.5$ at zero temperature, which is confirmed in Ref. [14] as well as supported in the discussion given in Sec. IV.

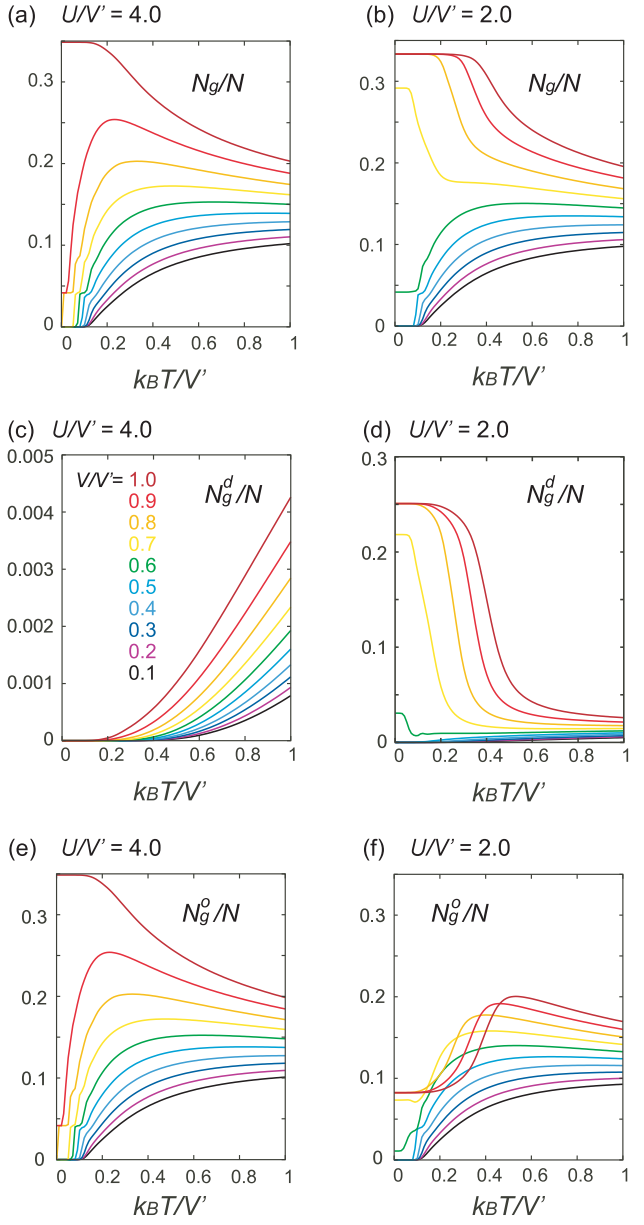

FIG. 8. (Color online) Temperature dependence of the number density of good defects (N_g/N) at (a) $U/V' = 4$ and (b) $U/V' = 2$ for $V/V' = 0.1 - 1$. In (c) and (d), the good defects with double occupancy (N_g^d/N), and in (e) and (f), those without double occupancy (N_g^o/N), are shown for comparison, where $N_g = N_g^o + N_g^d$.

approaches 1/3, which is the three-sublattice and contingent state [see Fig. 2(c)], included in the ground state manifold at $V = V'$.

Similar results are expected at sufficiently large U. Figure 8(a) shows the temperature dependence of N_g/N at $U/V' = 4$, which is in fact qualitatively the same as that of Fig. 7(a). However, when U becomes as small as $U/V' = 2$ [Fig. 8(b)], and V is close to V', N_g/N shows a rapid increase to 1/3 and stays there down to zero temperature. These $N_g/N = 1/3$ states correspond to the threefold CO phase we discussed earlier. Let us remind that in the present model, there is another series of good defects which has a doubly

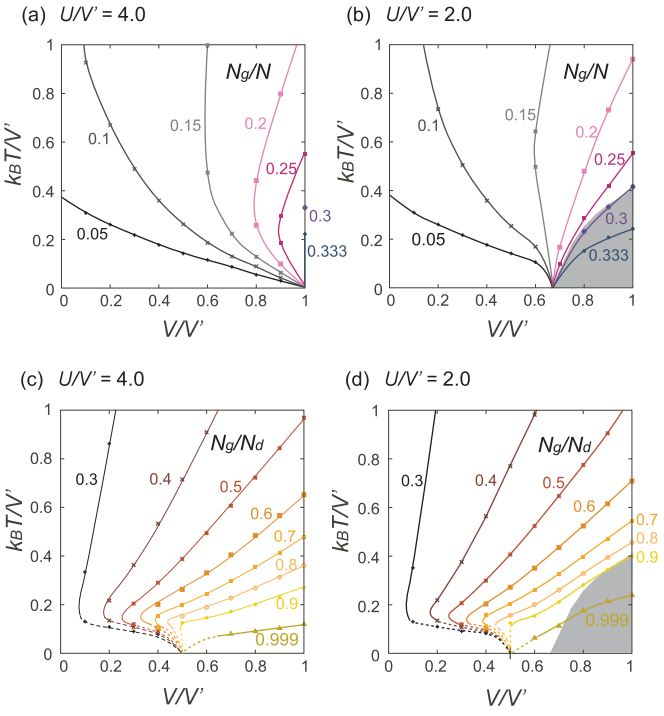

FIG. 9. (Color online) Contour plots of (a) and (b) the number density of good defect (N_g/N) and (c) and (d) the ratio of good defect to the total number of defects (N_g/N_d) at $U/V' = 4$ and 2. The broken line in (c) and (d) are the data whose finite size effect is not negligible, i.e., those in the region of $N_d/N \leqslant 2/48$, where the defect density is lower than the one available for the present cluster size.

occupied sites on their plaquettes [see Fig. 3(c)] in addition to the ones observed at $U = \infty$. We show in Figs. 8(c)–8(f) separately the number of good defects with(N_g^d) and without double occupancy(N_g^o). At $U = 2$, when entering the threefold CO phase at low temperature, N_g^d rapidly increases in the same manner as the double occupancy [Fig. 5(a)], and at the same time, N_g^o shows a sudden decrease. The values of these two kinds of good defects are something which we expect in the configuration in Fig. 3(a), $N_g^o/N = 1/12$ and $N_g^d/N = 1/4$. Figure 9 shows the contour plots of N_g/N and N_g/N_d; A bundle of contour lines of N_g/N flow into a single point at zero temperature, $V/V' = 1$ and ~ 0.7 for $U/V' = 4$ and 2, respectively, which corresponds to the onset of the $N_g/N = 1/3$ region. This region is stabilized at smaller U, and a long-range ordered threefold CO phase appears.

To see how the concentration of good defects are varied at around the phase transition point, we show in Fig. 10 N_g/N, N_g^d/N, N_g^o/N, and D as functions of both V and k_BT. The behavior of the double occupancy synchronize with that of the number of good defects with double occupancy, which means that the two states are classified by N_g^d/N_g.

IV. DISCUSSION

We show in Figs. 11(a) and 11(b) the phase diagram summarizing our results in the previous section. The ground

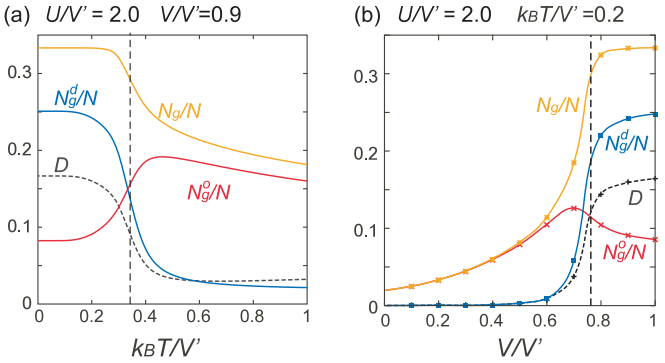

FIG. 10. (Color online) Number density of good defects and the double occupancy D, as functions of (a) temperature and (b) V near the phase transition to the threefold CO. For the good defects, the total number (N_g/N), the one with (N_g^d/N), and without double occupancy (N_g^o/N) are separately shown.

state at large enough U is basically a chain stripe [see Fig. 2(b)]. When U becomes small, the threefold charge order [see Fig. 3(a)] emerges near $V \sim V'$. Both of these states form manifolds of degenerate configurations; the chain stripe does not have double occupancy, and the particles form staggered order along the strong V' bonds, while the stripes formed along the otherwise directions are disordered. Similar type of partial disorder is also observed in the electron system on the nonfrustrated honeycomb lattice coupled to localized spins, where the frustration emerges due to the competing double exchange and superexchange interactions [35]. The threefold CO is a long range ordered phase based on three sublattice structure with two of them empty, and with the remaining sublattice occupied (half of the sites are doubly occupied).

At finite temperature, a series of "good defect states," which has slightly higher energy and larger degree of degeneracy than these ground states, appear as a consequesnce of the entropic gain of the free energy. In this state, the good defects each carrying the excitation energy of $(V' - V)/2$ are required to align alternatively between every neighboring two chains. Otherwise, they are replaced by bad defects with higher energies. As the good defects are allowed to move back and forth along the chain as far as they do not break the alignment rule, we could regard them as forming a soft dynamic network in a sea of staggard chain stripe, as illustrated schematically in Fig. 11(c).

Now, we explain the details of the phase diagram following the context of Ref. [14]. The good defect states are basically stabilized near $V \sim V'$ at low temperature where their excitation energy remains small. As the temperature rises, the bad defects are activated exponentially, $N_b/N_d \sim \mathrm{e}^{-T_b/T}$, and the system crossovers to the random 2D disordered phase. The crossover temperature, T_b, evaluated from the numerical data is given in broken line in Figs. 11(a) and 11(b). The good defect state also becomes unstable at smaller V, and again crossovers to the 1D disorder at $V \simeq V'/2$. This could be understood quite easily from the energetics; as shown in the left two panels of Fig. 11(d), depleting a pair of good defects on one chain at the center costs the energy of $2V - V'$, where the extra two good defects on the neighboring chains sandwiched by the depleted good defects are converted to

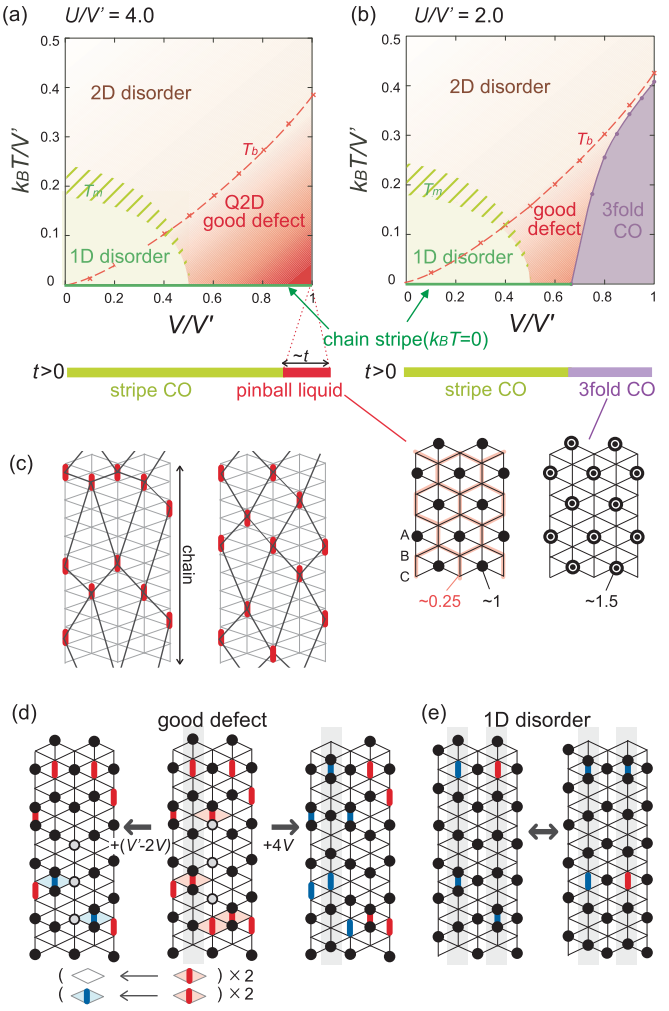

FIG. 11. (Color online) Phase diagram of the extended four state Potts model based on the numerical results at (a) $U/V' = 4$ and (b) $U/V' = 2$. Broken line(T_b) and the shaded region [T_m, which is ambiguous due to finite size effect, see Figs. 9(c) and 9(d)] indicate the crossover lines, which were not shown in Fig. 4. Solid line is the transition to the long-range ordered threefold CO phase. The pinball liquid and threefold CO phases realized at $t > 0$ are illustrated in the panels in the bottom right. (c) Schematic illustration of soft dynamic lattice structure based on the good defects(red bonds) in a sea of CO (particles are abbreviated) along the chain. The two configurations are the examples of degenerate manifolds of states with fixed N_d/N. (d) The depletion of a pair of good defects on the center chain, namely shifting the three bullets one site downwards, converts the good defect state in the middle panel to the left ones, increasing the energy by $2V - V'$, where two good defects disappear and other two good defects in the neighboring chain are converted to bad ones. Exchanging the particle occupation as $n_i = 0 \leftrightarrow 1$ along the shaded chain converts the middle panel to the right one, increasing the energy by $4V$. (e) Example of the 1D disordered state in the small V region of the phase diagram. Exchanging the particle occupation as $n_i = 0 \leftrightarrow 1$ along the shaded chains convert the left and right panels to each other without changing the energy.

bad ones. This means that at $V < V'/2$, the good defects are unstable and are depleted one by one. Then, both good and bad defects are generated independently on each chain, and we have a 1D disordered state; converting all the singly

occupied sites to the empty ones and vise versa over one chain with the particle number conserved, do not change the energy, regardless of whether the chain hosts defects or not. In Fig. 11(e), we actually show the example of converging two shaded chains independently. Therefore, in any of these 1D disordered states, each chain could freely choose two different configurations, so that the N_x chains altogether form a free 1D pseudo Ising spin system. Such picture does not hold in the good defect state; the defects could propagate only along the chain, while at the same time their locations are correlated between neighboring chains, which is the reason why we consider them as quasi-two-dimensional. In fact, if we convert the occupied and empty sites on a good defect chain as in the right panel of Fig. 11(d), the energy rises by $4V$. Therefore the good defect state is protected against the depleation and conversion, as far as $V > V'/2$.

The good defect state was originally proposed in the Ising model, namely the $U = \infty$ limit of the present model. There, a phase diagram similar to Fig. 11(a) is observed [14]. In the present model, we additionally consider another series of good defects which includes doubly occupied sites on a plaquette it belongs to [Fig. 3(b)], which has comparably low-energy with the original good defects when U is small enough. By counting the number of these defects separately as, N_g^o and N_g^d, against the total number of defects, N_d, one could understand the difference between the two phase diagrams, Figs. 11(a) and 11(b). At large U and $V \sim V'$, the good defect dominates the low-temperature phase, and with decreasing U, N_d increases mainly due to the contribution from those with double occupancy N_g^d. As U further decreases down to $\sim 2V + V'$, N_g^d rapidly increases and the good defect states undergoes a phase transition to the threefold CO phase. We indeed find that the energy difference of threefold CO state from the good defect state with $N_d/N = 1/3$ amounts to $(U - V' - 2V)/6$ (see Table I). In the threefold CO phase, the number of good defects become $N_d/N = (N_d^d + N_d^o)/N = 1/3$ at low k_BT.

The comparison of these results with the those of the extended Hubbard model at quarter-filling will help to understand the whole physical picture of this frustrated system. As pointed out in Ref. [19], the extended Hubbard model on a regular triangular lattice, $V = V'$, hosts two characteristic insulating state, the threefold CO and the pinball liquid, which are shown schematically in Fig. 11. In the former state, the number of particles on three different sublattices are approximately, $n_B = n_C = 0$ and $n_A = 3/2$, which gives $D \sim 1/6$ (here we describe the particle numbers in terms of the holes in the model of Ref. [19] dealing with 3/4-filling). This phase is realized at relatively small U ($\lesssim 2.5V - 3V$). As U increases, part of the particles on doubly occupied sites [a sublattice in Fig. 2(c)] spill out and become a separate fluid moving freely along the other two sublattices (B and C sublattices) with the particle distribution of $n_B = n_C = 1/4$ and $n_A = 1$.

As clearly seen from the comparison of particle density distribution, the threefold CO and pinball liquid phases of the extended Hubbard model correspond to our threefold CO and good defect states with $N_d/N \sim 1/3$, respectively. Starting from the strong coupling limit of Eq. (2), which is our extended four state Potts model, and by perturbatively introducing the t_{ij} term, the two states in our model are converted to the above mentioned two quantum phases [20,21,36], respectively. In our classical model, the spin degrees of freedom remain degenerate, so that all the states in the phase diagram are magnetically disordered. Introduction of t_{ij} usually lifts such degeneracy and the antiferromagnetic long-range order appears. The structure of magnetic ordering depends not only on the geometry of localized charges but also on t_{ij}, e.g., in the stripe CO at small V, the antiferromagnetic ordering takes place along the CO stripe, and at $V = V'$ and $t = t'$, a small magnetic moment on one sublattice with rich particle density in the pinball or threefold CO phase is expected to form a 120° Néel order as in the spin 1/2 Heisenberg model [37].

Notice that the good defect state is not a long-range order but a thermally activated phase that crossovers to the random disordered phase at higher temperature. The above mentioned quantum fluctuation, t_{ij}, transforms this disordered phase to the pinball liquid with long-range order of "pins" on A sublattice, which is a typical order-by-disorder phenomena discussed in Ref. [21].

As the two phases in both the classical and quantum cases are discriminated by rapid change (or a possible jump in the thermodynamic limit of the extended Hubbard model) in the double occupancy, we could interpret this transition as a partial and inverse Mott transition. Here, we call "inverse" because the metallic (pinball or good defect phase) phase becomes insulating (threefold CO) by the increase of double occupancy, which is contrary to the usual Mott transition.

Let us finally refer to the experimental studies on the organic solid, θ-$ET_2MZn(SCN)_4$ (M = Cs and Rb). The crystal of θ-ET_2X has an alternating layer of conducting ET molecules and insulating anions [38], and the ET molecules are aligned in an anisotropic triangular lattice geometry. Some of the materials with weaker frustration host a stripe CO at temperature lower than ~200 K [horizontal stripe in the left panel in Fig. 2(b)]. The metallic phase above this transition temperature is already unconventional, as the optical conductivity cannot be explained within the ordinary Drude type response of a normal metal [39]. θ-$ET_2CsZn(SCN)_4$, which possibly has a larger degree of frustration of V and V', falls off this insulating phase and shows weakly temperature independent resistivity down to low temperature, finally showing an upturn, which is considered as a sign of an incoherent (bad) metal. There, nonlinear conductance is observed [40], which is attributed to the competing two different types of short-range charge ordering of twofold (stripelike) and threefold in-plane periodicity [25]. Another material, θ-$ET_2RbZn(SCN)_4$, which lies at the phase boundary, is found to sustain this bad metallic character only when rapidly cooled down. The experimental evidence of spatial inhomogeneity of these two competing short-range orders on a nanometer scale was given by the x-ray diffraction measurement [41].

Recently, the dynamics of such possibly frustrated charges is measured by the resistance fluctuation spectroscopy on θ-$ET_2RbZn(SCN)_4$ [26]; the anomalous contributions off the $1/f$ noise from the resistance power spectrum density are extracted. They are attributed to the dynamics of charges, which slows down by the orders of magnitudes with decreasing temperature. Their temperature dependence also indicates the growth of heterogeneities charge clusters at the same time, which extend over ~25 triangular spacings, as indicated by the

x-ray diffraction measurement. These experimental findings suggest that the bad metallic behavior is caused by a rather classically disordered nature of charges, which is referred to as a charge glass. Examination of the charge-glass-forming ability of θ-ET_2X is systematically carried out with the aid of x-ray measurements, and the geometrical frustration is found to play crucial role to slow down the dynamics of charge ordering [42].

In fact, this glassy kind of disorders may be better described by the present extended four-state Potts model rather than its quantum version, an extended Hubbard model. The value of U and V of θ-ET_2X is not known. However, the *ab initio* density functional theory evaluates those of the reference system, κ-ET_2X [$X = \mathrm{Cu(NCS)_2}$ and $\mathrm{Cu_2(CN)_3}$] as $U/V \sim 2$–5, based on the constrained random phase approximation [43]. As the on-site Coulomb interaction generally depends only on the species of molecules, and the κ and θ type of molecular arrangement is not much different in their molecular packing density, we consider that this evaluation also holds of the θ-ET_2X as well. In fact, another organic material, TMTTF/TMTSF$_2X$, based on different molecules, has a similar ratio of U/V according to the optical measurements compared with theory, $U/t = 5$–7 and $V/t = 2$–3 [44]. Now, putting $U/V \sim 2$–5 into our phase diagram, we find that the possible charge glass state should correspond to a good defect state, as the threefold CO phase is stabilized only at smaller U. The good defect state is basically a disordered state but is not a simple disorder, so that it could be regarded as a kind of a short-range order slowly fluctuating along the chain direction. It is natural to expect that they freeze to a glassy state as the temperature is lowered if we consider the extra energy scale such as coupling with the phonons. While the threefold-like short-range order of θ-ET_2X has been often related to the threefold CO of the extended Hubbard model [16–18], we consider based the present discussion that it is much closer to the state between the pinball liquid and the good defect state. In fact, the transport measurements show that the relaxation time (aging behavior of resistance) of the charge glass of θ-$ET_2CsZn(SCN)_4$ follows an Arrhenius type of temperature dependence, indicative of a strong liquid, in which the rearrangement of charge configurations occurs locally [45]. This idea perfectly fits with the way the defects fluctuate locally along the chains.

V. SUMMARY AND OUTLOOK

We have studied the effect of thermal fluctuation on the frustrated electrons living on an anisotropic triangular lattice by taking the limit of zero quantum fluctuation, i.e., in the extended four state Potts model. The model consists of two species of classical particles with up and down spin indices, having four different states, (0),(↑),(↓), and (↑↓), per each lattice site. The particles on the same site interact with U and those on the neighboring site do via V' or V, with one bond direction being different from the other two. Off the fully frustrated case (i.e., $V \neq V'$), fixing the particle number to quarter-filling (one particle per two lattice sites) basically yields stripe charge ordered phases. Focusing on the parameter region with relatively large frustration, $V' \geqslant V$, we find that a manifold of low-energy states which we call "good defects" dominate the low-energy excitations levels of the model. In this state, the defects, namely, V' bonds breaking the charge ordering, follow the rule to align alternatively between neighboring V' chains. Their freedom to fluctuate freely along the chains without breaking this rule allows for macroscopic classical degeneracy. By the entropic gain of free energy due to this degeneracy, the good defects overtake the stripe ground state at finite temperature.

Our classical Monte Carlo calculation based on the Wang-Landau algorithm shows that the low temperature region of the model at $V' \sim V$ is indeed dominated by the "good defect" state at large U, where the model smoothly connects to the classical Ising model in which the good defect state was originally proposed [14]. As U is decreased, the good defect state undergoes a transition to the threefold CO phase at around $V \sim V'$, which could be regarded as a particular type of Mott transition characterized by the rapid change of the double occupancy of particles. The good defect state and the threefold CO phase are the analogues of the pinball liquid and the threefold CO of the extended Hubbard model at quarter filling, respectively, which are realized by intoducing the quantum fluctuation t to our model.

We argue that the glassy and strong liquid nature of the charges observed in a series of organic materials, θ-ET_2X, could be well understood by the "good defect" picture. How to characterize such state which is not simply disordered by defining the positive "order parameter" remains an issue to be studied.

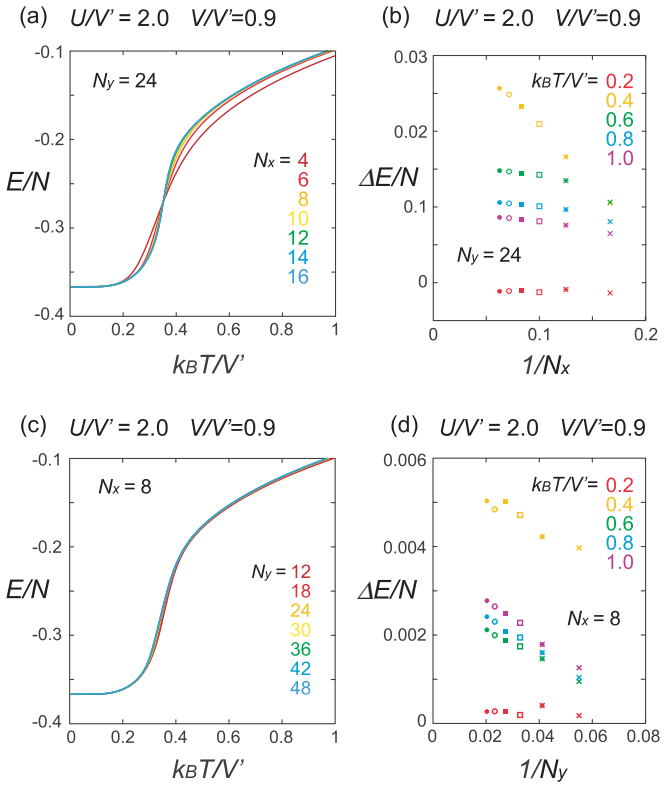

FIG. 12. (Color online) System size dependence of the energy density, E/N. (a) shows N_x dependences at fixed $N_y = 24$ and (b) the variation, $\Delta E = E(N_x, N_y = 24) - E(N_x = 4, N_y = 24)$, (c) N_y dependences at fixed $N_x = 8$, and (b) the variation, $\Delta E = E(N_x = 8, N_y) - E(N_x = 8, N_y = 12)$.

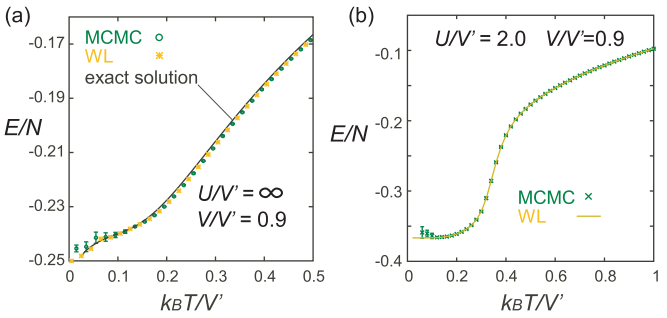

FIG. 13. (Color online) (a) Comparison of the energy of the exact solution of the Ising model (solid line) with the MCMC and WL results at $U = \infty$ and $V/V' = 0.9$. (b) Comparison between the MCMC and WL at $U/V' = 2$ and $V/V' = 0.9$. In both cases, we set $N_x \times N_y = 8 \times 24$, and the statistical averages of MCMC is taken over 20 independent runs each with 5000 MCS.

ACKNOWLEDGMENTS

This work is supported by Grant-in-Aid for Scientific Research (No. 25800204) from the Ministry of Education, Science, Sports and Culture of Japan.

APPENDIX A: ACCURACY OF THE RESULTS

As we discussed in Sec. III A, we adopted the WL method since the statistical error at low temperature is reasonably small compared to MCMC. Whereas, the size of the cluster available is limited. We examined the size dependence of the results before determining the cluster size we adopted, namely, $N_x \times N_y = 8 \times 24$ and 8×48. Figure 12 shows the N_x and N_y dependencies of the energy at $U/V' = 2$ and $V/V' = 0.9$, which is the parameter where the WL method has the worst convergence. As we can see, the N_y dependence is almost negligible, whereas we need to take $N_x \geqslant 8$ to have the energy almost converged to that of the bulk limit. The variation of energy, ΔE, compared to its extrapolated value in the bulk limit, deviates the largest near $k_B T \sim 0.4V'$, which is the region where the good defect state sets in.

The accuracy of WL results is examined in Fig. 13. In the $U = \infty$ limit, we have the exact solution of the Ising model, and the WL results show reasonably good agreement even at $N_x \times N_y = 8 \times 24$ down to lowest temperature. By contrast, the MCMC method starts to show deviation at $k_B T/V' \lesssim 0.1$. A similar tendency is observed at $U/V' = 2$ [Fig. 13(b)], while we do not have an exact solution for this parameter.

APPENDIX B: DENSITY OF STATES

The WL method provides us with the density of states, Ω, which enables us to understand the low-energy structure of the model. Figure 14 shows Ω/N as functions of E/N for several choices of parameters, corresponding to the results we obtained in the main text. Here, we classified the states without double occupancy in green, and the good defect state which includes those with and without double occupancy in red. One finds that the lowest energy part of Ω/N are dominated by the good defect states. The profile of Ω scales well with N, namely Ω/N does not depend much on N.

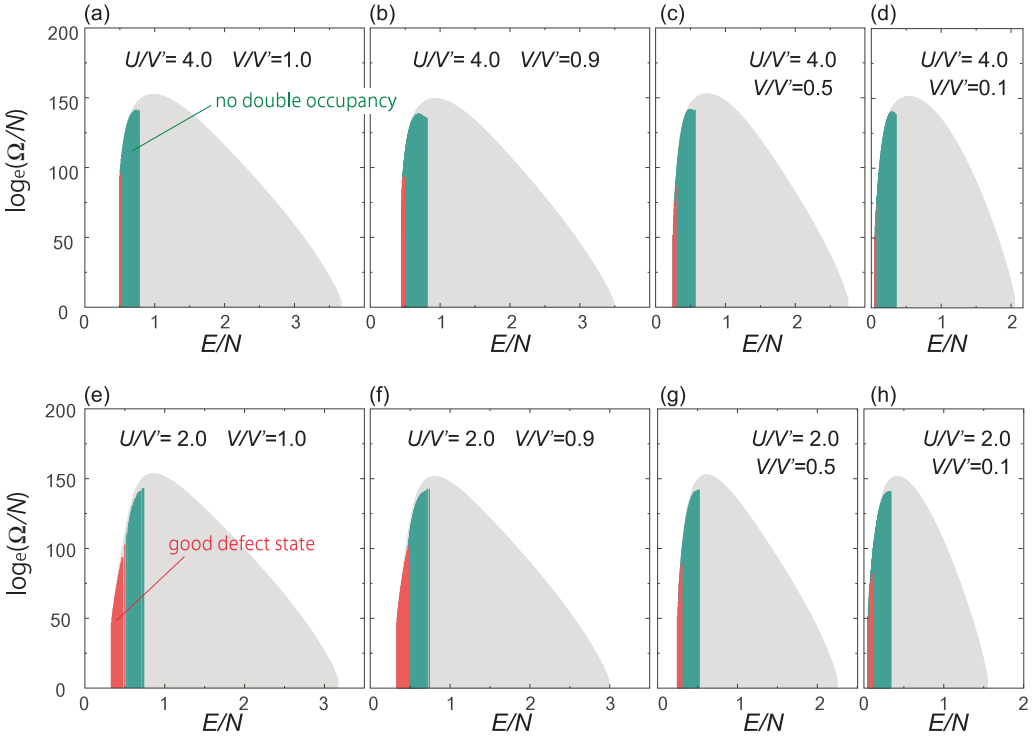

FIG. 14. (Color online) Density of states per site, Ω/N, obtained by the WL method. The variation of $U/V' = 4$ and 2, $V/V' = 1, 0.9, 0.5, 0.1$ are shown for $N_x \times N_y = 6 \times 24$. The profile of Ω/N basically does not depend on N, namely the logarithmic density of states scale well with N.

[1] *Frustrated Spin Systems*, edited by H. T. Diep (World Scientific, Singapore, 2004) and the references therein.

[2] L. Balents, Nature (London) **464**, 199 (2010) and the references therein.

[3] N. Shannon, T. Momoi, and P. Sindzingre, Phys. Rev. Lett. **96**, 027213 (2006).

[4] V. Cannella and J. A. Mydosh, Phys. Rev. B **6**, 4220 (1972).

[5] K. Binder and A. P. Young, Rev. Mod. Phys. **58**, 801 (1986).

[6] J. Villain, Z. Phys. B: Condens. Matter **33**, 31 (1979).

[7] H. Kawamura, Phys. Rev. B **38**, 4916 (1988).

[8] M. J. P. Gingras, in *Spin Ice, in Highly Frustrated Magnetism*, edited by C. Lacroix, P. Mendels, and F. Mila (Springer, Berlin, 2010).

[9] C. Hotta, Crystals **2**, 1155 (2012).

[10] J. Villain, R. Bidaux, J.-P. Carton, and R. Conte, J. Phys. **41**, 1263 (1980).

[11] R. B. Potts, Math. Proc. **48**, 106 (1952).

[12] G. H. Wannier, Phys. Rev. **79**, 357 (1950).

[13] R. M. F. Houtappel, Physica **16**, 425 (1950).

[14] C. Hotta, T. Kiyota, and N. Furukawa, Europhys. Lett. **93**, 47001 (2011).

[15] M. Sato, N. Watanabe, and N. Furukawa, J. Phys. Soc. Jpn. **82**, 073002 (2013).

[16] J. Merino, H. Seo, and M. Ogata, Phys. Rev. B **71**, 125111 (2005).

[17] H. Watanabe and M. Ogata, J. Phys. Soc. Jpn. **75**, 063702 (2006).

[18] S. Nishimoto, M. Shingai, and Y. Ohta, Phys. Rev. B **78**, 035113 (2008).

[19] L. Cano-Cortés, J. Merino, and S. Fratini, Phys. Rev. Lett. **105**, 036405 (2010).

[20] L. Cano-Cortés, A. Ralko, C. Février, J. Merino, and S. Fratini, Phys. Rev. B **84**, 155115 (2011).

[21] C. Hotta and N. Furukawa, Phys. Rev. B **74**, 193107 (2006).

[22] T. Devakul and R. P. Singh, Phys. Rev. B **90**, 125136 (2014).

[23] J. Merino, A. Ralko, and S. Fratini, Phys. Rev. Lett. **111**, 126403 (2013).

[24] K. Miyagawa, A. Kawamoto, and K. Kanoda, Phys. Rev. B **62**, R7679 (2000).

[25] F. Sawano, I. Terasaki, H. Mori, T. Mori, M. Watanabe, N. Ikeda, Y. Nogami, and Y. F. Noda, Nature (London) **437**, 522 (2005).

[26] F. Kagawa, T. Sato, K. Miyagawa, K. Kanoda, Y. Tokura, K. Kobayashi, R. Kumai, and Y. Murakami, Nat. Phys. **9**, 419 (2013).

[27] θ-$ET_2CsM(SCN)_4$ (M = Zn, Co) shows coexisting two different types of short-range order with wave number, $\boldsymbol{q}_1 = (2/3,k,1/3)$, and $\boldsymbol{q}_2 = (0,k,1/2)$, both with nanometer correlation length scale [28–30]. Here, a and c of the crystal coordinate, (a,b,c), correspond to x and y of the present two-dimensional model, respectively. Similar coexisting short-range orders are observed also in θ-$ET_2RbZn(SCN)_4$ at $T \geqslant 200$ K (below which the stripe long-range order due to $\boldsymbol{q}_2$ appears), while with different wave number $q_1' = (1/3,k,1/4)$ [31,32].

[28] Y. Nogami, J.-P. Pouget, M. Watanabe, K. Oshima, H. Mori, S. Tanaka, and T. Mori, Synth. Met. **103**, 1911 (1999).

[29] M. Watanabe, Y. Nogami, K. Oshima, H. Mori, and S. Tanaka, J. Phys. Soc. Jpn. **68**, 2654 (1999).

[30] T. Ito, M. Watanabe, K. Yamamoto, N. Ikeda, Y. Nogami, Y. Noda, H. Mori, T. Mori, and I. Terasaki, Europhys. Lett. **84**, 26002 (2008).

[31] M. Watanabe, Y. Noda, Y. Nogami, and H. Mori, J. Phys. Soc. Jpn. **73**, 116 (2004).

[32] M. Watanabe, Y. Noda, Y. Nogami, and H. Mori, J. Phys. Soc. Jpn. **74**, 2011 (2005).

[33] M. Udagawa and Y. Motome, Phys. Rev. Lett. **98**, 206405 (2007).

[34] F. Wang and D. P. Landau, Phys. Rev. E **64**, 056101 (2001).

[35] J. W. F. Venderbos, M. Daghofer, J. van den Brink, and S. Kumar, Phys. Rev. Lett. **107**, 076405 (2011).

[36] C. Hotta, N. Furukawa, A. Nakagawa, and K. Kubo, J. Phys. Soc. Jpn. **75**, 123704 (2006).

[37] B. Bernu, C. Lhuillier, and L. Pierre, Phys. Rev. Lett. **69**, 2590 (1992).

[38] H. Mori, S. Tanaka, and T. Mori, Phys. Rev. B **57**, 12023 (1998).

[39] H. Tajima, S. Kyoden, H. Mori, and S. Tanaka, Phys. Rev. B **62**, 9378 (2000).

[40] K. Inagaki, I. Terasaki, H. Mori, and T. Mori, J. Phys. Soc. Jpn. **73**, 3364 (2004).

[41] Y. Nogami, N. Hanasaki, M. Watanabe, K. Yamamoto, T. Ito, N. Ikeda, H. Ohsumi, H. Toyokawa, Y. Noda, and I. Terasaki, J. Phys. Soc. Jpn. **79**, 044606 (2010).

[42] T. Sato, F. Kagawa, K. Kobayashi, A. Ueda, H. Mori, K. Miyagawa, K. Kanoda, R. Kumai, Y. Murakami, and Y. Tokura, J. Phys. Soc. Jpn. **83**, 083602 (2014).

[43] K. Nakamura, Y. Yoshimoto, T. Kosugi, R. Arita, and M. Imada, J. Phys. Soc. Jpn. **78**, 083710 (2009).

[44] F. Mila, Phys. Rev. B **52**, 4788 (1995).

[45] T. Sato, F. Kagawa, K. Kobayashi, K. Miyagawa, K. Kanoda, R. Kumai, Y. Murakami, and Y. Tokura, Phys. Rev. B **89**, 121102(R) (2014).